Aerodynamic and Aeroacoustic Effects of Swirl Recovery Vanes Length

Avallone, Francesco; van den Ende, Luc; Li, Qingxi; Ragni, Daniele; Casalino, Damiano; Eitelberg, Georg; Veldhuis, Leo

DOI
10.2514/1.C035552

Publication date
2019

Document Version
Accepted author manuscript

Published in
Journal of Aircraft: devoted to aeronautical science and technology

Aerodynamic and Aeroacoustic Effects of Swirl Recovery Vanes Length

F. Avallone *, L. van den Ende †, Q. Li ‡, D. Ragni §, D. Casalino ¶, G. Eitelberg ‖ and L. Veldhuis **
Faculty of Aerospace Engineering, Delft University of Technology, Kluyverweg 1, 2629HS, Delft, The Netherlands

A numerical investigation of a propeller with swirl recovery vanes (SRVs), for which experimental data exist, is performed. A second SRV geometry, with shorter vanes to avoid the impingement of the propeller tip vortices, is also investigated. For the baseline SRVs, the efficiency of the propulsive system increases of 2.4% with respect to the isolated propeller. This is obtained by converting angular momentum in axial momentum. A reduction of the swirl angle in the near wake by 48% is found. Most of the thrust is generated at the root of the vanes. Leading-edge impingement noise is the dominant source. The vanes cause noise increase by 20 dB with respect to the isolated propeller in the axial direction, where noise from the propeller vanishes. In the axial direction, sound pressure level spectra show tonal peaks at harmonics of the second blade passing frequency (BPF) while, in the other directions, peaks are present at harmonics of the first BPF. However, the overall isolated propeller noise is 23 dB higher than the noise generated by the SRVs. Shortening the vane length causes 13% reduction of the thrust generated by the vanes with respect the baseline case, but no variation of the far-field noise.

Nomenclature

c	=	chord [m]
C_T	=	thrust coefficient [-]
D	=	propeller diameter [m]
J	=	advance ratio [-]
n	=	rotational velocity [rev/s]
P	=	power [W]
r	=	local blade radius [m]

*Assistant Professor, AWEP Dept., f.avallone@tudelft.nl, AIAA member.
†MSc., AWEP Dept., lvandende@gmail.com.
‡PhD candidate, AWEP Dept., q.li-2@tudelft.nl, AIAA member.
§Assistant Professor, AWEP Dept., d.ragni@tudelft.nl, AIAA member.
¶Full Professor, AWEP Dept., d.casalino@tudelft.nl, AIAA member.
‖Full Professor, AWEP Dept., g.eitelberg@tudelft.nl, AIAA member.
**Full Professor, AWEP Dept., l.l.m.veldhuis@tudelft.nl, AIAA member.

R = blade radius [m]

T = thrust [N]

V_a = axial velocity component [m/s]

V_t = tangential velocity component [m/s]

V = velocity [m/s]

Greek symbols

β = pitch angle [degree]

η = efficiency [-]

λ_2 = criterion for vortex visualization [s^{-2}]

ω = angular velocity [rad/s]

ϕ = phase angle [degree]

φ = swirl angle [degree]

ρ = density [kg/m^3]

θ = azimuth angle [degree]

ζ = local chordwise coordinate [m]

Subscript

$prop$ = propeller

r = root

srv = swirl recovery vane

t = tip

∞ = free-stream

Superscript

$-$ = time-average

I. Introduction

Aircraft propulsion systems based on propellers are well known for their relatively higher propulsive efficiency with respect to turbofan. This is due to the higher mass-flow rate and lower exhaust velocity [1], that permit a reduction of fuel consumption of approximately 10% [2]. The propulsive efficiency can be further increased converting angular momentum into axial momentum by installing a second row of blades downstream of the propeller. These blades can rotate (Contra-Rotating Open Rotor, CROR) [3] or be stationary (Swirl Recovery Vanes, SRVs) [1, 4]. The lower weight and complexity of the SVRs, particularly because of the absence of moving components, make them more attractive than CROR.

Since SRVs generate additional thrust by changing the direction of the momentum flux, their design and integration in the full propulsion system needs careful attention [5, 6]. As a matter of fact, if not well designed, they can even cause a reduction of the propulsive efficiency [6, 7] due to their extra drag.

The main design challenge is to account for the complex unsteady fluid dynamics of rotor/stator interaction. Both the impingement of the propeller wake on the SRVs and the upstream effect of the SRVs on the propeller shall be taken into account. In the wake of the propeller, a turbulent flow and tip vortices are present; they impinge on the SRVs causing unsteady variation of both lift and drag during one propeller revolution [8]. For this reason, the impingement, deformation and convection of the propeller wake and tip vortex helix on the SRVs [9] shall be considered. Once the tip vortex helix impinges on the vane, it splits over the two sides of the vane; the splitted vortices convect downstream following different trajectories to finally merge at the trailing edge [10] where an additional interaction with the SRVs' tip vortex might happen depending on the length of the SRVs [5]. The variation of the flow field due to the deformation of the wake can have an additional upstream effect on the propeller inflow, showing unsteady pressure fluctuations with frequencies that depend on the number of SRVs [1].

For a propeller-SRVs propulsion system, few unsteady experimental data are available in the literature. The most detailed dataset has been collected by Sinnige et al. [1]. The authors combined experimental measurements with unsteady Reynolds Averaged Navier-Stokes (RANS) simulations to investigate both aerodynamics and aeroacoustics. The propulsive efficiency increased of 0.7% with respect to the isolated propeller even if stall occurred at the root of the SRVs. The increase of aerodynamic performance, obtained by recovering 46% of the rotational kinetic energy, resulted in noise increase up to $3-5$ dB at high thrust setting and 7 dB at low thrust setting. Noise increase was associated to the tonal peaks at higher harmonics of the Blade Passing Frequency (BPF) caused by the impingement of the slipstream on the SRVs [11]. No increase of broadband noise was found. The acoustic results of Sinnige et al. [1] differ from the experimental findings of Dittmar and Hall [12], who reported no noise increase caused by the SRVs.

Aim of this manuscript is to report the investigation of the aerodynamic flow field and the aeroacoustic far-field noise for a propeller-SRVs configuration, previously optimized for performance using a lifting line theory, for which experimental reference data are available [5]. Lattice-Boltzmann Very Large Eddy Simulations (LB-VLES) coupled with the Ffwocs Williams and Hawkings (FWH) integral solution are carried out using the same configuration of Li et al. [5]. This represents the first dataset where both the aerodynamic and the acoustic fields are retrieved using a single tool, thus allowing to link far-field noise with the unsteady aerodynamics. For further characterization of the flow mechanisms, the baseline SRVs are modified by shortening the vanes, to avoid the impingement of the propeller tip vortices on the vanes.

In the following, the descriptions of the computational setup, of the geometry and of the adopted methodology are reported in section II. The computational setup is validated in section III by comparing the numerical results against experimental and RANS data. Aerodynamic and acoustic results for the baseline configuration and the one with shorter

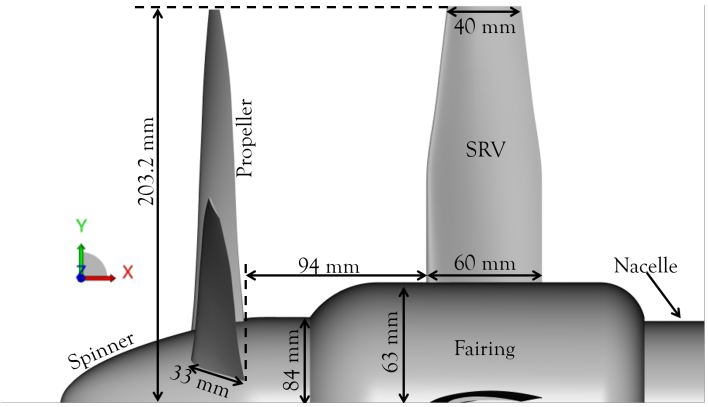

Fig. 1 Geometry of the propeller with installed swirl recovery vanes.

vanes are reported in sections IV and V, respectively. The main findings of this work are summarized in the conclusions.

II. Computational setup

A. Geometry

The propeller geometry [5] equipped with the SRVs is shown in figure 1. The propeller is a 1:9 scaled-model of a Dowty Rotol propeller, used on the IPTN N-250. It features six blades and a diameter D of 0.4064 m. The hub of the propeller is 0.084 m in diameter, the root chord c_r is 33 mm and the blade pitch angle β equals 30° at 70% of the radius R. The SRVs are positioned on a fairing of diameter $0.31D$. Their leading edge is at 94 mm behind the propeller trailing edge at the root. The SRV chord is 60 mm at the root ($c_{r,SRV}$) and 40 mm at the tip ($c_{t,SRV}$). The vanes were modeled with the lifting line theory using as input the velocity field from RANS simulations by Li et al. [5] where the optimal circulation distribution was determined by maximizing the thrust of the vanes. The nacelle extends until the end of the domain to avoid any re-circulation in the back and mimic the wind tunnel support of the propeller.

The free-stream velocity V_∞ is set at 29 m/s and the propeller advance ratio $J = V_\infty/nD$ is 0.6, where $n = 119$ rev/s is the rotational velocity in revolutions per second. For this configuration, an additional increase of 2.620% of thrust is expected based on the measurements of Li et al. [5]. To free-stream turbulence is set to 0.5% to match the reference experiments and computations.

Even if it is known that shorter vanes do not generate as much thrust as the longer ones (i.e. the interaction between the tip vortex and the vanes has a relevant effect) [5], a second configuration with shorter SRVs is investigated to evaluate the influence of tip-vortex/vane interaction on the radiated noise. They are obtained by shortening the vanes to an outer radius of $0.84D$ to avoid direct impingement of the blade tip vortex on the SRVs.

A reference system centered at the propeller plane, with x-axis oriented in the axial downstream direction and y and z axis oriented such to form a left-hand oriented reference system, is adopted.

B. Methodology

The LB method is chosen because it has been validated for aerodynamics and aeroacoustics studies for similar phenomena [11, 13–16]. Its implementation in the commercial software 3DS-Simulia PowerFLOW 5.4b is used. For a detailed description of the method, the reader can refer to Succi [17] and Shan et al. [18], while to Chen [19] for a review.

The LB method solves the Boltzmann equation on a Cartesian mesh, named as lattice. The discretization used for this particular application consists of 19 discrete velocities in three dimensions (D3Q19), involving a third-order truncation of the Chapman-Enskog expansion. It was shown that this scheme accurately approximates the Navier-Stokes equations for a perfect gas at low Mach number in isothermal conditions [20]. The equations are solved with an explicit time integration approach and the stability of the solution is obtained with a unitary Courant-Friedrichs-Lewly (CFL) number. To obtain the particle distribution, a collision term, based on a unique Galilean invariant [21], and an equilibrium distribution of Maxwell-Boltzmann [20] are adopted.

A VLES model is implemented to take into account the effect of the sub-grid unresolved scales of turbulence. Following Yakhot and Orszag [22], a two-equations $k-\epsilon$ renormalization group is used to compute a turbulent relaxation time that is added to the viscous relaxation time. In order to reduce the computational cost, a pressure-gradient-extended wall-model is used to approximate the no-slip boundary condition on solid walls [23, 24]. The model is based on the extension of the generalized law-of-the-wall model [25] to take into account the effect of the pressure gradient.

The compressible and time-dependent nature of the transient numerical solution together with the low dissipation and dispersion properties of the LB scheme allow extracting the sound pressure field directly in the near-field up to a cut-off frequency corresponding to approximately 15 voxels per acoustic wavelength. In the far field, noise is computed by using the FWH equation [26]. The formulation 1A, i.e. a solution of the Ffowcs Williams-Hawkings (FW-H) equation, developed by Farassat [27] and extended to a convective wave equation, is used in this study [28, 29]. The formulation is implemented in the time domain using a source-time dominant algorithm [30].

C. Computational volume and boundary conditions

The simulation volume is defined as a rectangle with a length of $25.7D$ and a width and height of $15D$. The center and origin are defined by the intersection of the propeller axis with the propeller plane. At the inlet, a velocity boundary condition with velocity equal to V_∞ is set. At the outlet, the pressure is set to the ambient pressure 101,325 Pa. At the other edges of the domain, free-stream velocity boundary conditions are set. No-slip boundary conditions are applied on the propeller, SRVs, spinner and fairing. A free-slip boundary condition is applied to the nacelle which extends to the outlet plane. A volume of revolution is generated containing the propeller and spinner with a clearance from the surfaces of 19 mm.

Twelve variable resolution (VR) regions are used (figure 2). The resolution increases by a factor of two from one

Fig. 2 Distribution of the variable resolution (VR) regions in the near field.

VR region to the next. The finest region (VR12) is defined by an offset of $0.030c_r$ from regions around the leading edge (LE, in orange), trailing edge (TE, green) and the tip (blue) of both the propeller and vanes to capture the high surface curvature and the accompanying pressure peaks accurately. The region around the propeller TE has been added in order to capture the shape of the trailing edge accurately. A similar discretization is adopted around the SRVs. The VR regions around the tip of the SRVs have been extended in spanwise direction to capture the propeller tip vortex development over the SRVs accurately. For both the propeller and SRVs, the LE and TE regions are defined to be approximately 10% of the local chord. The propeller tip region has a similar size and the vane tip region has a spanwise length of $0.08D$.

An acoustic sponge is implemented by exponentially varying the kinematic viscosity per unit temperature from 0.005 m^2/sK at $3.3D$ up to 0.5 m^2/sK at $4.9D$. This is adopted to avoid that spurious reflections from the edge of the domain contaminate the acoustic sampled data. Simulations are seeded with the end result of the preceding simulation with a coarser grid.

III. Grid independence study and comparison with experiments

The grid independence study and the comparison with the computational and experimental results from Li et al. [5] are reported in this section. First, the isolated propeller configuration, or SRVs OFF case, is analyzed to ensure that the main flow features are well captured. Then, the case with the baseline SRVs installed, or SRVs ON case, is presented.

A. Isolated propeller

The time-averaged thrust coefficient for the isolated propeller $\overline{C_{T\,prop}}$, defined as:

$$\overline{C_{T\,prop}} = \frac{\overline{T}_{prop}}{\rho_\infty n^2 D^4}, \tag{1}$$

and the Overall Sound Pressure Level (OSPL), expressed in dB using a reference pressure of 20×10^{-6} Pa, are used as integral parameters for the convergence analysis. In equation 1, $\overline{T}_{prop}$ is the time-averaged thrust generated by the propeller, ρ_∞ is the free-stream density and n is the rotational speed in revolutions per second. OSPL is computed using

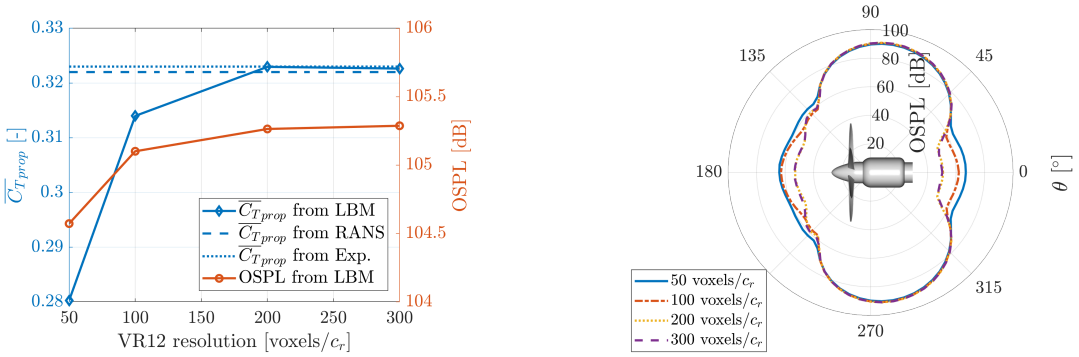

Fig. 3 Grid convergence study for the isolated propeller configuration. Four grid resolutions, expressed as voxels per root chord are investigated. (left) Time-averaged thrust coefficient $\overline{C_T}$ and Overall Sound Pressure Level (OSPL) for θ equal to 90° at a distance of 20R. (right) Directivity pattern of OSPL at a distance of 20R.

the FWH analogy on a ring with radius 20R and centered at $x/D = 0.2$. Both quantities are plotted in figure 3 (left) for four grid resolutions, expressed as voxels per propeller blade root chord in the most refined region (i.e., VR12). The four grids are obtained by increasing the resolution of all the VR regions in the computational domain. In the same figure, reference data from computations and experiments are reported [5] as constant $\overline{C_{Tprop}}$ lines. In figure 3 (right), the OSPL directivity patterns for the four grids are also plotted to ensure that also far-field data converge. For the far-field noise, no reference measurement is available.

Both $\overline{C_{Tprop}}$ and OSPL at $\theta = 90°$ show an underestimation with respect to the experimental data for low grid resolutions. Grid convergence is achieved for a resolution of 200 voxels/c_r for both quantities. An excellent agreement with the reference data, both experimental and computational, is obtained for the $\overline{C_{Tprop}}$. On the contrary, for low grid resolution an overestimation of the OSPL for angles in the range $-30° < \theta < 30°$ and $150° < \theta < 210°$ is found. For the OSPL, the maximum difference between the two finest grids is 1.4 dB for θ equal to 205°.

The assessment is extended to the time-averaged near-wake velocity field to ensure that the wake is well captured. In figure 4 (top), profiles of both the time-averaged axial $\overline{V_a}$ and tangential $\overline{V_t}$ velocity components at $x/D = 0.24$ are plotted for the four grid resolutions. For the resolution of 200 voxels/c_r, the comparisons against experiments and RANS are reported in the bottom row. The experimental uncertainty is indicated by the yellow band.

Results show only minor differences between the two finest resolution cases for $0.4 < r/R < 0.5$. This is attributed to the fact that by using the finest grid, smaller structures are better captured particularly in the slipstream of the propeller. However, the variations can be considered negligible and the comparison with the reference experimental and computational data shows good agreement. Only an overestimation of the tangential velocity component, but smaller than 3% of V_∞, is found.

Convergence for the resolution of 200 voxels/c_r for the isolated propeller configuration is further confirmed by the comparison of the non-dimensional time-averaged pressure distribution at 70% of the propeller blade radius reported in figure 5, where the local coordinate over the chord is indicated with ζ. The time-averaged pressure is

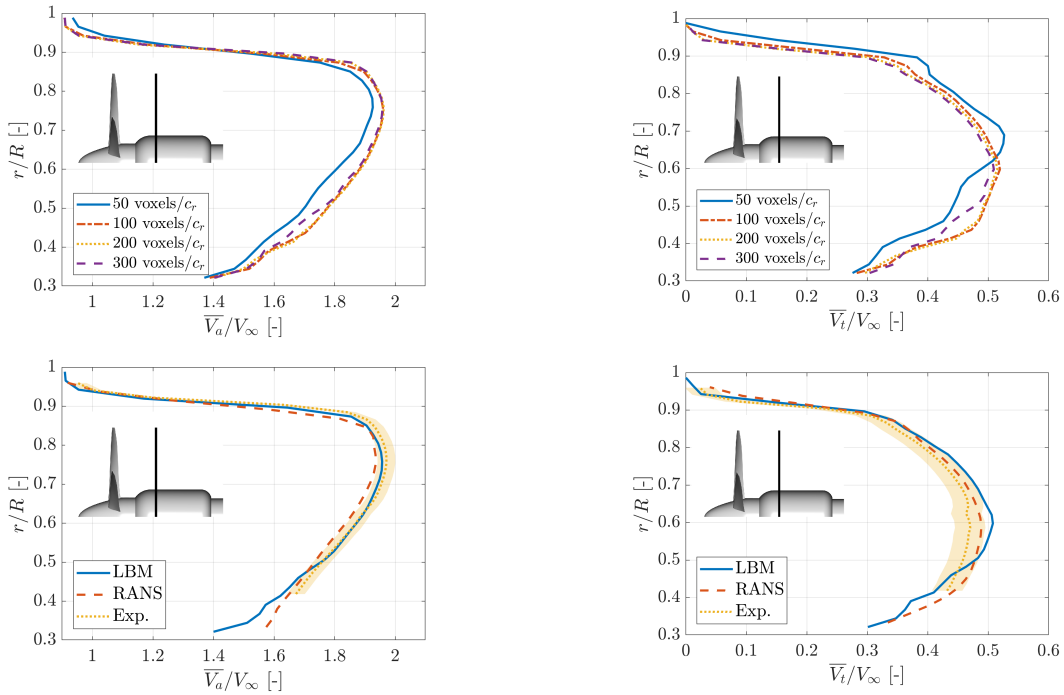

Fig. 4 Grid convergence study for the isolated propeller configuration. Four grid resolutions, expressed as voxels per root chord are investigated. Dependence of the time-averaged axial velocity component $\overline{V_a}$ (top left) and tangential velocity component $\overline{V_t}$ (top right) on the grid resolution. For the resolution of 200 voxels/c_r, the comparison with experiments and RANS for the same quantities is reported in the bottom figures. Data are extracted at $x/D = 0.24$ as indicated by the black line.

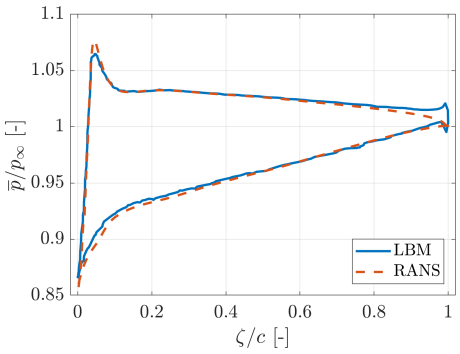

Fig. 5 Comparison of the time-averaged pressure distribution obtained from LB method for a resolution of 200 voxels per root chord with the RANS simulations.

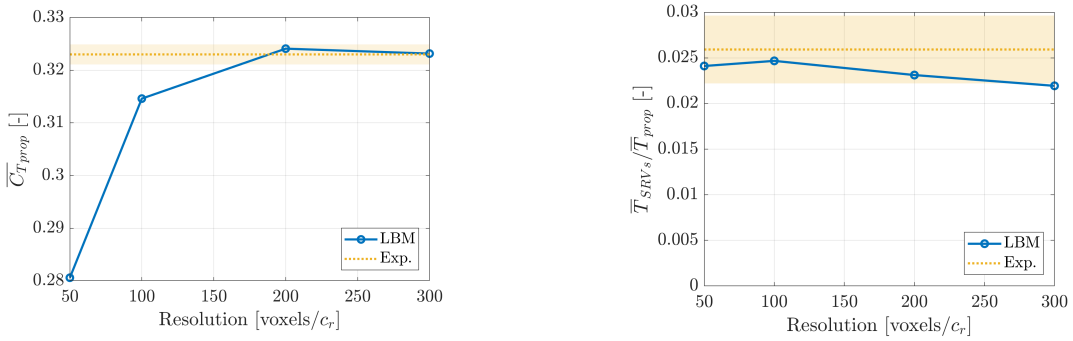

Fig. 6 Grid convergence study for the propeller with the SRVs. Four grid resolutions, expressed as voxels per root chord are investigated. (left) Time-averaged thrust coefficient of the propeller $\overline{C_{T_{prop}}}$. (right) Ratio of the time-averaged thrust generated by the swirl recovery vanes and the propeller $\overline{T}_{SRVs}/\overline{T}_{prop}$. Results are compared against experimental results.

non-dimensionalized with respect to the free-stream dynamic pressure p_∞. The small difference near the stagnation point can be attributed to the lower resolution of the LB simulation (minimum y^+ equal to 12) with respect to the RANS (y^+ equal to 1); the differences at the trailing edge are attributed instead to a small difference in the geometry between the two simulations (i.e., the trailing edge for the LB simulations is blunter than in the RANS).

B. Propeller with swirl recovery vanes

The convergence study is carried out also for case with the SRVs installed. For this configuration, grid convergence is verified using the time-averaged thrust coefficient of the propeller $\overline{C_{T_{prop}}}$, and the ratio between the time-averaged thrust generated by the SRVs and the one generated by the propeller ($\overline{T}_{SRVs}/\overline{T}_{prop}$). Results are reported in figure 6 where they are also compared with experimental results. Similarly to above, the experimental uncertainty is indicated by the yellow band.

As for the previous configuration, convergence is reached for resolution equal to 200 voxels/c_r. No major variation in the convergence of $\overline{C_{T_{prop}}}$ is found with respect to the isolated configuration. The contribution of the SRVs,

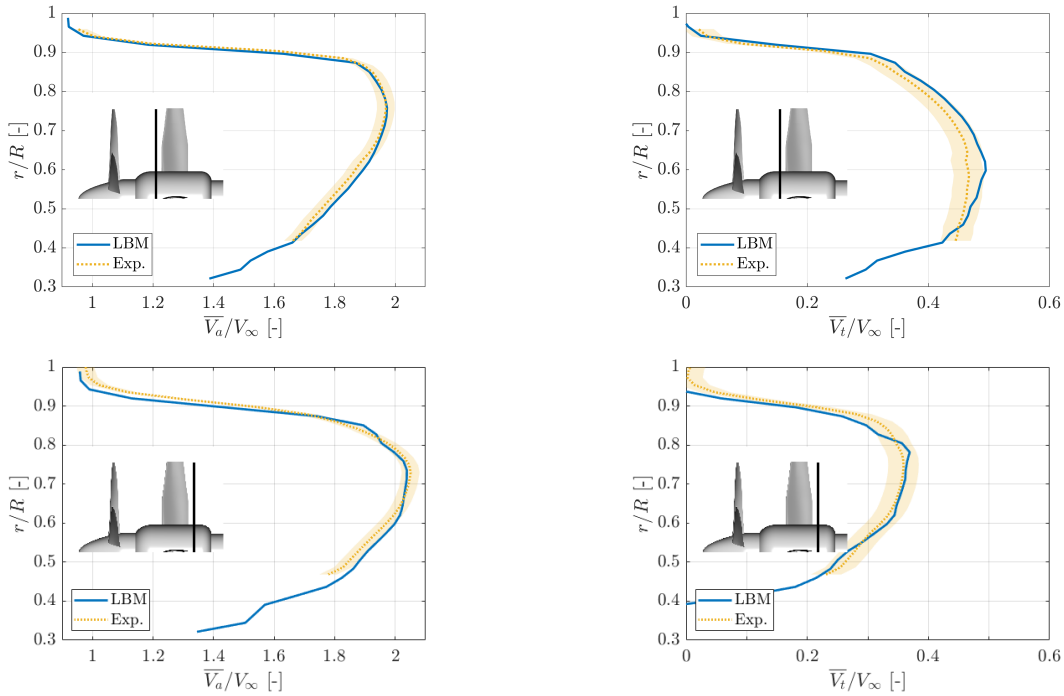

Fig. 7 Comparison of the time-average axial $\overline{V_a}$ and tangential $\overline{V_t}$ velocity components upstream (top) and downstream (bottom) of the swirl recovery vanes ($x/D = 0.24$ and $x/D = 0.45$, as indicated by the black lines) between the computational results obtained for the resolution of 200 voxels/c_r and the experiments.

which generated about 2% of the time-averaged thrust generated by the propeller, shows that the integral effects of the impingement are well captured with the resolution of 200 voxels/c_r.

The suitability of the discretization strategy is further confirmed by the comparisons of the time-averaged velocity components obtained from computations with the experimental ones. Both $\overline{V_a}$ and $\overline{V_t}$ are plotted at $x/D = 0.24$ (upstream of the SRVs) and $x/D = 0.45$ (downstream of the SRVs) respectively in the top and bottom row of figure 7. A very good agreement is found between the two datasets. The figure further shows that the flow across the SRVs increases $\overline{V_a}$ and decreases $\overline{V_t}$, i.e. thrust is generated converting angular momentum in axial momentum.

The grid independence is further assessed for the installed configuration plotting the directivity plots of the OSPL at $20R$ for different resolutions in figure 8. As for the isolated case, and similarly to what found for the $\overline{T}_{SRVs}$, convergence is reached for the 200 voxels/c_r resolution, which shows variation smaller than 1 dB with respect to the 300 voxels/c_r resolution case.

IV. Baseline configuration

A. Aerodynamics

The influence of the SRVs on the aerodynamic performances of the propulsion system is evaluated in terms of integral quantities such as time-averaged thrust coefficient $\overline{C_T}$, time-averaged torque coefficient $\overline{C_Q}$ and propulsive

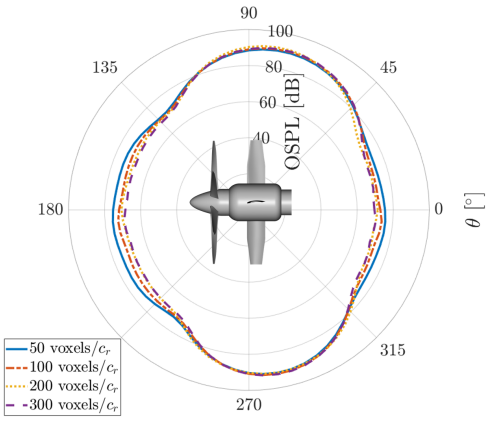

Fig. 8 Grid convergence study for the propeller with the SRVs. Four grid resolutions, expressed as voxels per root chord are investigated. Directivity pattern of OSPL at a distance of 20R.

	Isolated Propeller	Propeller + SRVs
$\overline{C_{T\,Prop}}$	0.3235	0.3241 (+0.19%)
$\overline{C_{Q\,Prop}}$	0.0546	0.0546 (+0.08%)
η_{Prop}	0.5658	0.5664 (+0.10%)
$\overline{C_{T\,SRVs}}$	-	0.0078
η_{tot}	0.5658	0.5794 (+2.40%)

Table 1 Comparison of the time-averaged thrust coefficient $\overline{C_T}$, time-averaged torque coefficient $\overline{C_Q}$ and propulsive efficiency η for the isolated propeller and the propeller with SRVs. The subscripts $Prop$ and $SRVs$ refer to the data obtained for each of the two components.

efficiency $\eta = \overline{T}V_\infty/\overline{P}$. They are summarized in table 1, where these parameters are listed for the isolated propeller and the case with SRVs. In the same table, the subscripts $Prop$ and $SRVs$ refer to the contribution of each component, while the subscripts tot refers to the full propulsion system.

Results show that the installation of SRVs increases the propulsive efficiency η_{tot} by 2.4%. This is due to additional thrust generated by both the SRVs and the propeller. The propeller time-averaged thrust coefficient $\overline{C_{T\,Prop}}$ increases by 0.19%, thus confirming an upstream effect of the SRVs on the propeller as also found experimentally [1]. A drawback of the installation of the SRVs is that the additional thrust is not constant in time but shows large fluctuations, as shown in figure 9 where the instantaneous C_T as a function of the phase angle ϕ is reported. These fluctuations might cause structural problems if not accounted for. For this particular case, the amplitude of the fluctuations is 0.24% of the time-averaged $\overline{C_T}$ and its frequency is 2 BPF ($\Delta\phi = 30°$), because of the presence of 6 propeller blades and 4 vanes. The periodic impingement of the propeller wake on the SRVs induces an additional unsteady upstream effect on the propeller that shows a more fluctuating C_T (figure 9 right) with respect to the case without SRVs.

As discussed previously, the additional thrust is obtained by changing the direction of the momentum flux in the slipstream of the propeller. To quantify the amount of swirl recovered through the installation of the SRVs, the axial

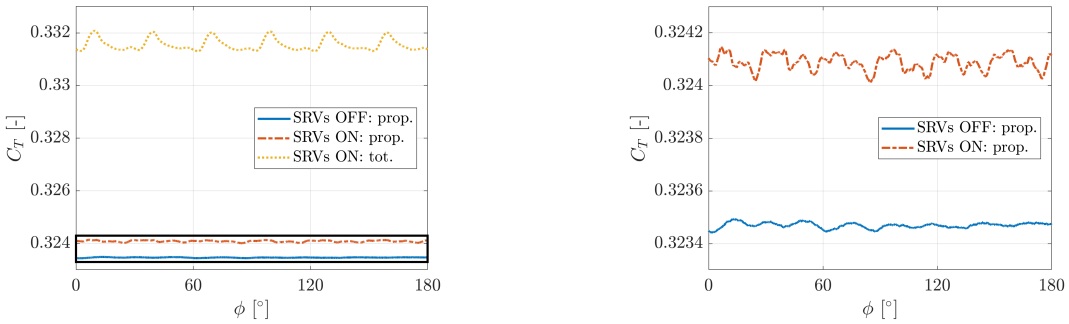

Fig. 9 Instantaneous thrust coefficient C_T versus the phase angle ϕ during a propeller rotation for both the isolated propeller and the case with installed SRVs. Both the propeller-only and total thrust is illustrated for the SRVs case. The figure on the left contains a rectangle which indicates the axis limits of the one on the right.

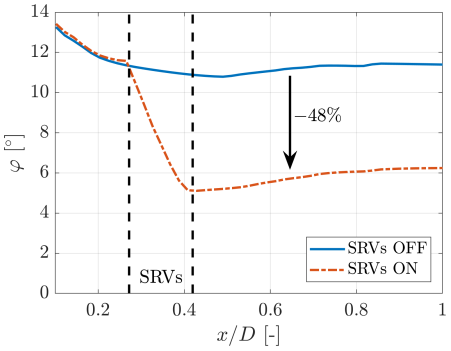

Fig. 10 Average swirl angle φ for the installed (SRVs ON) and the isolated propeller (SRVs OFF) configurations along the axial direction.

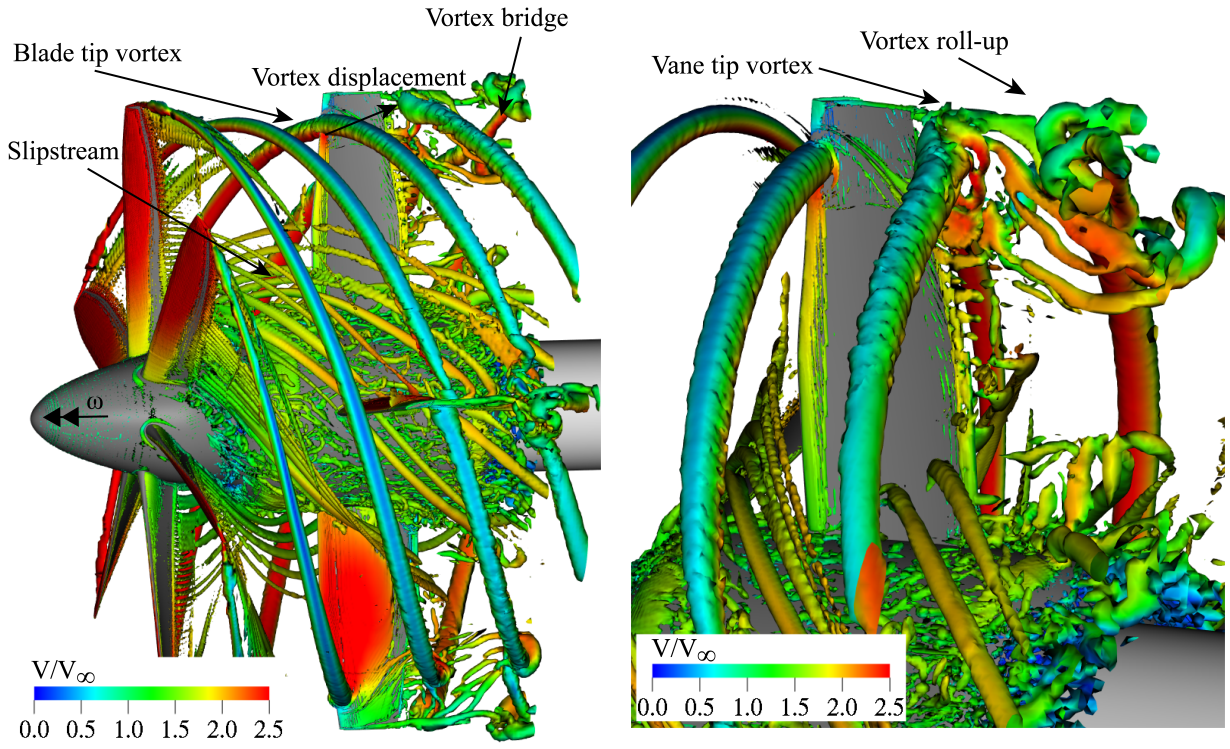

Fig. 11 Two views of the instantaneous flow field visualized through the λ_2 criterion for vortex visualization color contoured with the non-dimensional velocity magnitude V.

distribution of the swirl angle φ, averaged in the radial direction, is plotted in figure 10. Results show that the SRVs weakly alter the distribution of φ upstream of the vanes' leading edge. The swirl angle gradually decreases along the SRV's chord and, at the SRV's trailing edge, it increases in the axial direction up to a constant value equal to 6°. In the wake of the SRV, the swirl angle reduces by 48% with respect to the isolated propeller case.

The wake re-alignment is the cause of the reduction of φ and, as a consequence, of the improvement of the aerodynamic performance. To investigate the physics involved in the interaction, instantaneous flow visualizations through iso-surfaces of the λ_2 criterion for vortex identification, color-contoured with the non-dimensional velocity magnitude are plotted in figure 11. Two views of the same time instant are shown for clarity. Figures show that first the slipstream impinges at the root of the SRV and then the tip vortex impinges near the tip. This is caused by the sweeped leading edge of the SRVs and, mainly, by the fact that the tip vortex and the slipstream travel with different axial velocities (figure 7). Since the tip vortex travels with a lower velocity than the rest of the slipstream, a time delay between the two phases of the impingement exists. The axial velocity difference (i.e., about two times) is such that the tip vortex generated by a propeller blade impinges immediately before the slipstream associated to the following propeller blade (figure 11 left). As a consequence, each SRV generates unsteady thrust as shown in figure 12, where the instantaneous thrust coefficient of a single vane $C_{T_{SRV}}$ as a function of the phase angle ϕ for a propeller rotation is plotted. In the same figure, the swirl angle φ measured at $r/R = 0.7$ (i.e., where the slipstream impinges) and $x/D = 0.24$ (i.e., upstream

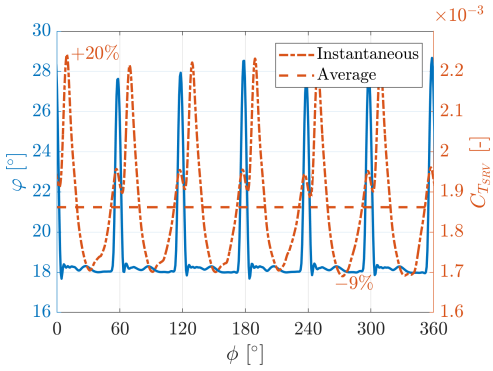

Fig. 12 (red) Thrust coefficient of single vane $C_{T_{SRV}}$ as a function of the phase angle ϕ during a propeller rotation. (blue) Swirl angle φ at $r/R = 0.7$ and $x/D = 0.24$.

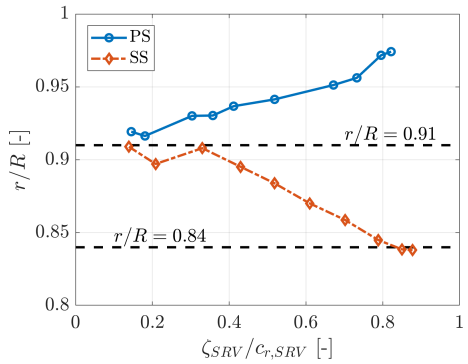

Fig. 13 Spanwise displacement of the blade tip vortex over the two sides of the swirl recovery vane surface.

of the SRV) is shown in blue. Results highlight two peaks: the first small peak corresponds to the impingement of the tip vortex generated by a propeller blade, while the second one corresponds to the impingement of the slipstream generated by the following propeller blade. The effect of the wake slipstream is larger because the increase of swirl angle associated with it (i.e., an increase of the local angle of attack seen by each SRV) affects a larger portion of the SRV. The periodic features in the wake cause a variation of the inflow angle of 10°. This causes an unsteady increase of 20% of the $C_{T_{SRV}}$ followed by a decrease, thus causing a maximum fluctuation of 29%.

Once the tip vortex helix impinges on the leading edge of the SRV, it splits over the two sides of the wing; the vortex filaments travel in the downstream direction along two different trajectories: toward the root at the propeller advancing side (i.e., suction side) and toward the tip at the propeller retraining side (i.e., pressure side) [1, 15]. The radial location of the split vortices on the SRV surface is shown in figure 13. The two vortices show a relative displacement of about 10%R while convecting over the SRV. At the trailing edge of the SRV, the vortex convecting over the retraining side of the SRV interacts with the SRV's tip vortex, while the other one rolls up because of the shear forces caused by the velocity gradient in the wake of the SRV (figure 11). The two vortices, subjected to these strong deformations, reconnect downstream where also the roll-up of the main vortex is clearer. This confirms that, even if optimized, residual rotational

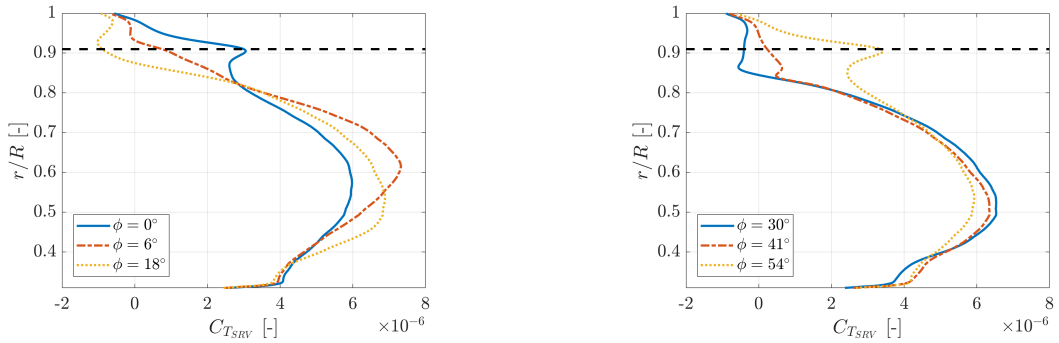

Fig. 14 Sectional thrust coefficient $C_{T_{SRV}}$ distribution over a single vane in the radial direction for different phase angles ϕ.

kinetic energy associated with the swirl, is still present in the wake, particularly in the tip vortex.

Figure 12 has shown that the peak of $C_{T_{SRV}}$ is associated to the slipstream impinging on the SRV and that the root of the SRV contributes to most of the aerodynamic performance increase. This is better shown in figure 14, where the thrust coefficient at each radial section of the SRV is plotted for different phase angles. The horizontal dashed line is the location of the blade tip-vortex impingement. Results show a dependence of the $C_{T_{SRV}}$ on the phase angle and that most of the thrust is generated for $r/R < 0.8$. The tip of the SRV contributes positively to the $C_{T_{SRV}}$ only when there is direct impingement of the blade tip vortex ($\phi = 0°$, figure 12). This is associated to the time-varying pressure imbalance between the suction and the pressure side of the SRV caused my the motion of the two vortices originated by the blade tip vortex (figure 13).

The complex flow field associated with the convection of the vortices on the SRV causes strong variations of the surface pressure distribution, thus creating a time-varying lift distribution with the appearance of separated flow regions. This is visualized in figure 15 where the phase-locked pressure distributions at the location of the tip vortex impingement $r/R = 0.91$ for three phase angles are plotted. The local axial coordinate on the SRV (ζ_{SRV}) is non-dimensionalized with respect to the local chord of the SRV (c_{SRV}). It evidences that the convection of the tip vortex along two directions creates a strong imbalance of the pressure forces over the two sides. Since this happens at the tip of the SRV, each SRV is subjected to a strong unsteady bending moment that needs to be accounted for in the design phase.

B. Acoustics

The impingement of the propeller blade on the SRVs has a direct effect on the far-field noise because of the introduction of an additional noise generation mechanism: leading-edge impingement. The directivity plot of the Overall Sound Pressure Level (OSPL) on a sphere of radius $20R$ and centered at $x/D = 0.2$ is plotted in figure 16 for the full propulsive system (left) and for each component (right). Data are plotted for both the SRVs ON and OFF cases and are integrated between 0.5 BPF and 10 BPF.

The installation of the SRVs has an effect on noise only in the axial direction ($-30° < \theta < 30°$ and $120° < \theta < 240°$)

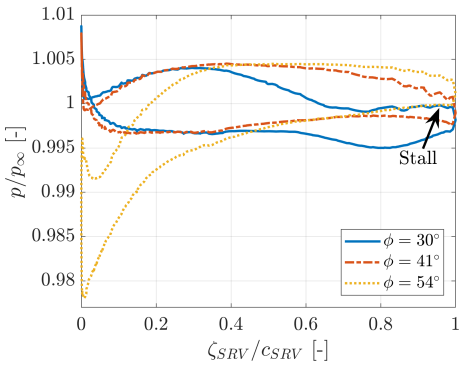

Fig. 15 Phase-averaged pressure distribution on the SRV at the radial location $r/R = 0.91$.

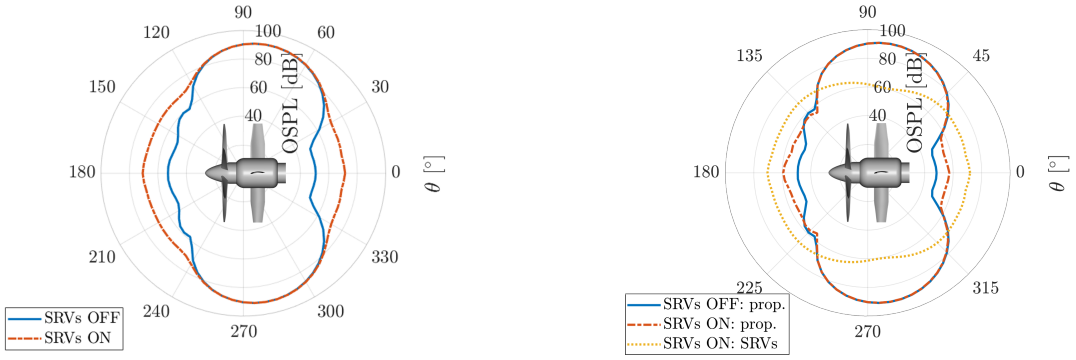

Fig. 16 Directivity plot of the Overall Sound Pressure Level (OSPL) computed on a sphere of radius $20R$ and centered at $x/D = 0.2$. Data are plotted for both the SRVs ON and OFF cases and are integrated between 0.5 BPF and 10 BPF. (left) Full propulsive system and (right) separate contribution of each component.

with an increase of the OSPL up to 20 dB. In the other angular directions, where the SRVs OFF case shows the largest noise amplitude, the effects of the SRVs installation are negligible. The decomposition of the contribution of each component of the propulsive system (figure 16 right) shows that the installation of SRVs has also an effect on the noise generated by the propeller. This cannot be associated to the higher $\overline{C_T}_{Prop}$ generated by the propeller due to the upstream aerodynamic effect (table 1) because, in this case, an increase in noise in all the directions is expected. Conversely, it suggests that the noise increase associated to the propeller might be caused by acoustic interference. However, the contribution of the propeller is negligible with respect to the SRVs one in the range of θ where noise increase is found for the full propulsive system. The noise directivity pattern associated with the SRVs is almost uniform for all the angles θ because of the effect of multiple dipole sources.

The discussion of the aerodynamic results has shown how the different parts of the SRVs contribute to the thrust coefficient and how they are involved in the propeller-wake-SRVs interaction. To determine the acoustic consequences of the interaction, the OSPL directivity plots for each component of the SRVs are plotted in figure 17. They are obtained by splitting the surface of the SRV blade as shown in the left figure and applying for each of them the FWH solid acoustic analogy. Figure 17 shows that vane leading edge, i.e. the region interested by the impingement of the propeller wake

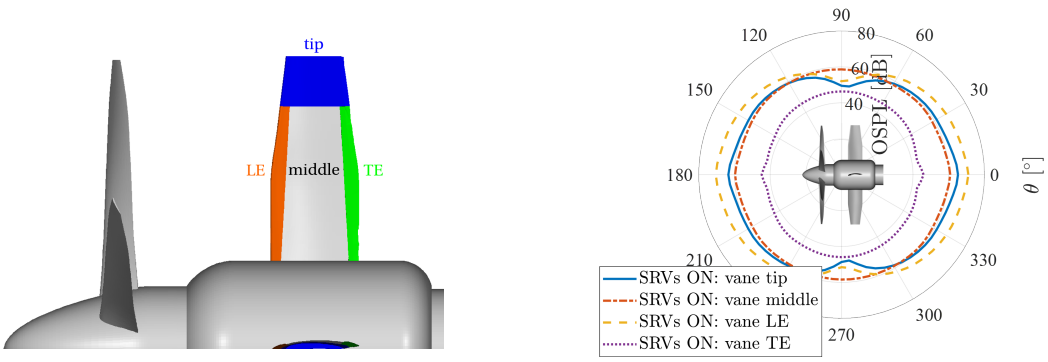

Fig. 17 Contribution of each part of the SRV to the directivity plot of the Overall Sound Pressure Level (OSPL) computed on a sphere of radius $20R$ and centered at $x/D = 0.2$. Data are integrated between 0.5 BPF and 10 BPF.

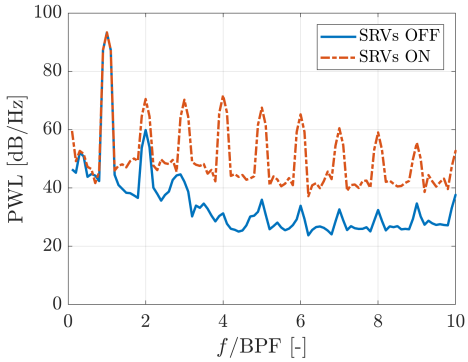

Fig. 18 Sound Power Level (PWL) as a function of frequency non-dimensionalized with respect to the blade passing frequency (BPF).

slipstream, is the one that contributes the most to the far-field noise with a dipole-like distribution in agreement with leading edge impingement noise. The middle part of the vane shows a more uniform pattern because of the existence of multiple dipole sources due to the impingement. The tip of the vane, subjected to the propeller tip vortex impingement, contributes less than the leading edge part to the OSPL, in agreement with the aerodynamic results discussed before. In this case, the vortices are still coherent while convecting on the blades thus justifying why the contribution of the vane trailing edge is negligible with respect to the rest of the vane.

To investigate the effect of the SRVs at different frequencies, Sound Power Level (PWL) as a function of the non-dimensional frequency is plotted for the two configurations in figure 18. As expected, results show a dominant tone at the first BPF with an almost exponential decay at higher harmonics. The SRVs do not affect the tone of the first BPF, which is associated with the propeller, but they amplifies all the tones associated to the higher harmonics and increase broadband noise as well. It is worth to mention that the power of the tone associated with the first BPF is 20 dB higher than the second one, so that it can be stated that the installation of the SRVs do not have any relevant effect on the total PWL perceived by a listener.

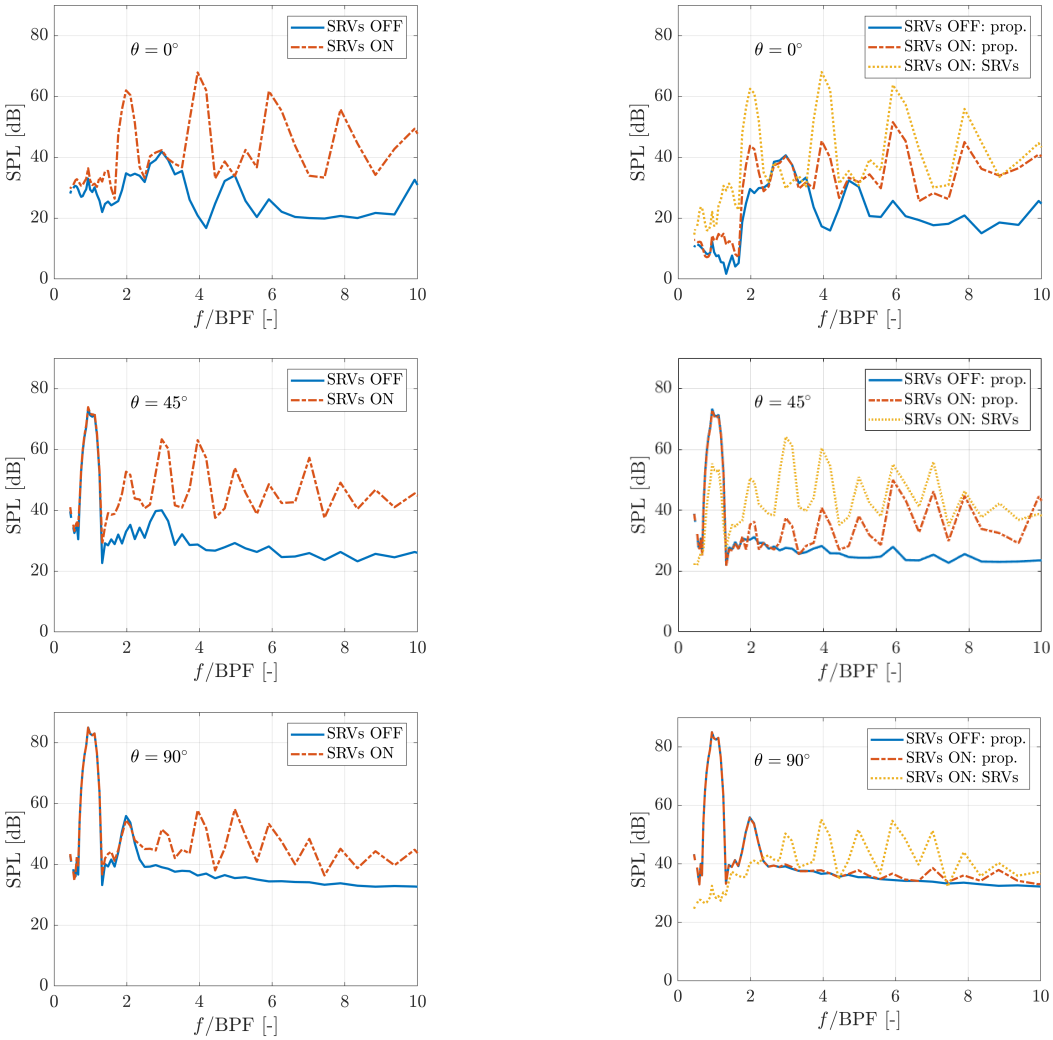

Fig. 19 Sound Pressure Level (SPL) in $1/12^{th}$ octave bands. On the left the comparison between SRV ON and OFF case is shown, while on the right the contribution of each component of the propulsion system is plotted.

The SPL plots in $1/12^{th}$ octave bands at different polar angles, plotted in figure 19, show how the different components of the propulsion system contribute to the far-field noise. On the left column of the figure, the comparison between the isolated propeller (SRVs OFF) and the installed configuration (SRVs ON) is reported, while on the right column the contribution of each component of the propulsion system is shown. In the axial direction $\theta = 0°$ (the same is found for $\theta = 180°$ but not plotted for the sake of conciseness), where the isolated propeller generates almost no noise, the dipole nature of impingement noise is dominant (figure 17); the configuration with SRVs shows tonal peaks at harmonics of the second BPF. The investigation of the dilatation fields, not shown here for the sake of conciseness, shows that it is caused by destructive interference between the acoustic waves generated at the leading edge of the vanes and from the upstream propeller. As already mentioned before, the presence of the SRVs has also an upstream effect on the propeller that generates tonal peaks not present for the isolated case. For other polar angles, where tonal noise associated with the propeller is dominant, it is evident that the acoustic interference is not present anymore and tonal peaks associated with the leading-edge impingement noise are found at harmonics of the first BPF. Since in figure 17 it was observed that at these polar angles the contribution of the middle part of the vane becomes dominant, this component of the tonal noise can be associated with the convection of the vortices over the blade while the turbulent nature of the slipstream can explain the increase of the broadband noise.

V. Shorter vane configuration

A second geometry with shorter vanes is investigated to study the effect of the propeller tip-vortex interaction on the aerodynamic and acoustic fields, motivated by the fact that most of the $\overline{C_T}$ is generated at the root, while the tip contributes only to noise at high polar angles. The vanes are cut such that the outer radius is equal to 0.84 R to avoid tip-vortex impingement. The rest of the geometry and free-stream conditions are the same.

Shortening the SRVs length has a negligible effect on the $\overline{C_T}$ of the upstream propeller that reduces by 0.01% but it has a relevant effect on the performance of the full propulsion system. Figure 20 shows the phase-locked thrust coefficient of a single vane $C_{T_{SRV}}$ as a function of the phase angle ϕ for a propeller rotation and for both the long and short vane configurations. The fact that the propeller tip vortex does not impinge on the SRVs leads to the absence of the first of the two peaks shown previously in figure 10. Because of the shorter vanes, the time-average $\overline{C_T}_{SRV}$ reduces by 13% with respect to the long vanes thus being equal to 2% of the propeller thrust. The thrust reduction is larger than the thrust associated to the the tip region ($r/R > 0.84$) for the baseline vanes that is equal to 1.9% of the total thrust generated by the vane.

Even if the tip of the baseline SRV contributes weakly to the overall $\overline{C_T}$, its presence has an effect on the flow development over the entire SRV. This is shown in figure 21 where the radial distributions of the phase-locked sectional thrust coefficient C_T for two phase angles are plotted for the shorter vane and the baseline case. Results show inboard reduction of the C_T for the shorter vane particularly at the tip region where a negative C_T is found. This is caused by

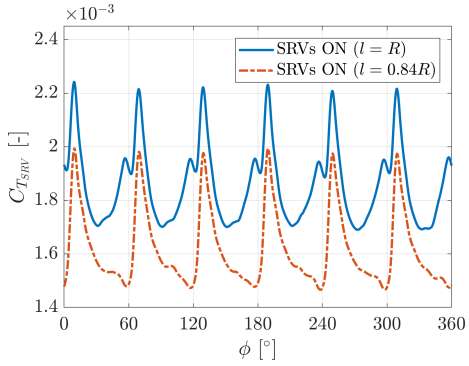

Fig. 20 Thrust coefficient of single vane $C_{T_{SRV}}$ as a function of the phase angle ϕ for a propeller rotation for the long and short vane configurations.

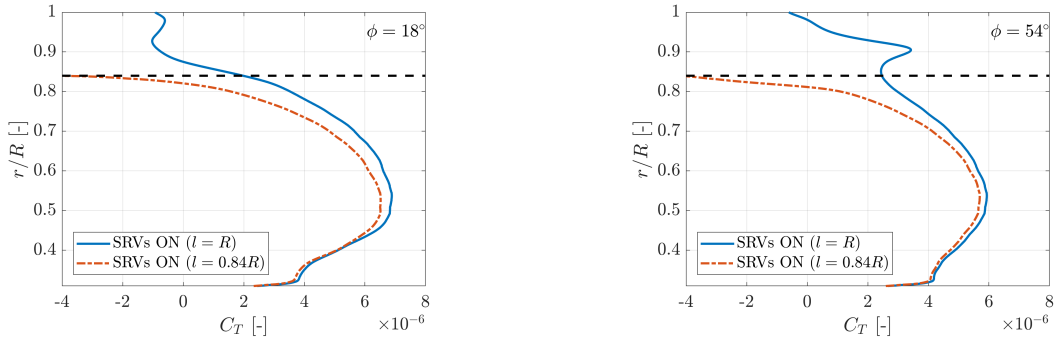

Fig. 21 Sectional thrust coefficient $C_{T_{SRV}}$ distribution over a single vane in the radial direction for two phase angles ϕ.

the generation of a stronger vane tip vortex (figure 22) with respect to the baseline case. The interaction between the propeller blade tip vortex and the vane tip vortex happens only downstream of the vane where the propeller blade tip vortex is deformed by the velocity field induced by the vane tip vortex. The rotation of the latter pushes the propeller tip vortex away from the vane on the retreating side and toward the vane on the advancing side. However, the distance and the relative strength is such that, for the current configuration, no breakdown of the propeller blade tip vortex is observed.

Since the propeller tip vortex does not interfere with the SRV, the residual swirl angle in the wake of the SRV is larger than in the previous case as shown in figure 23. Similarly to the previous configuration, no difference is found upstream of the SRV leading edge while a reduction is visible downstream. In this case, the SRVs reduces 13% less swirl angle with respect to the baseline case, in line with the $\overline{C_T}$ results discussed before (figure 20).

Comparing the radial distribution of the time-averaged swirl angle ϕ for the two configurations (figure 24), it is confirmed that SRVs tend to extract most of the energy from the slipstream of the wake and not from the propeller tip vortex [1]. This explains why the SRV should be long enough to interfere with the propeller blade tip vortex to redirect as much momentum as possible [31].

The aerodynamic results confirmed that shorter vanes are not beneficial from an aerodynamic perspective. To

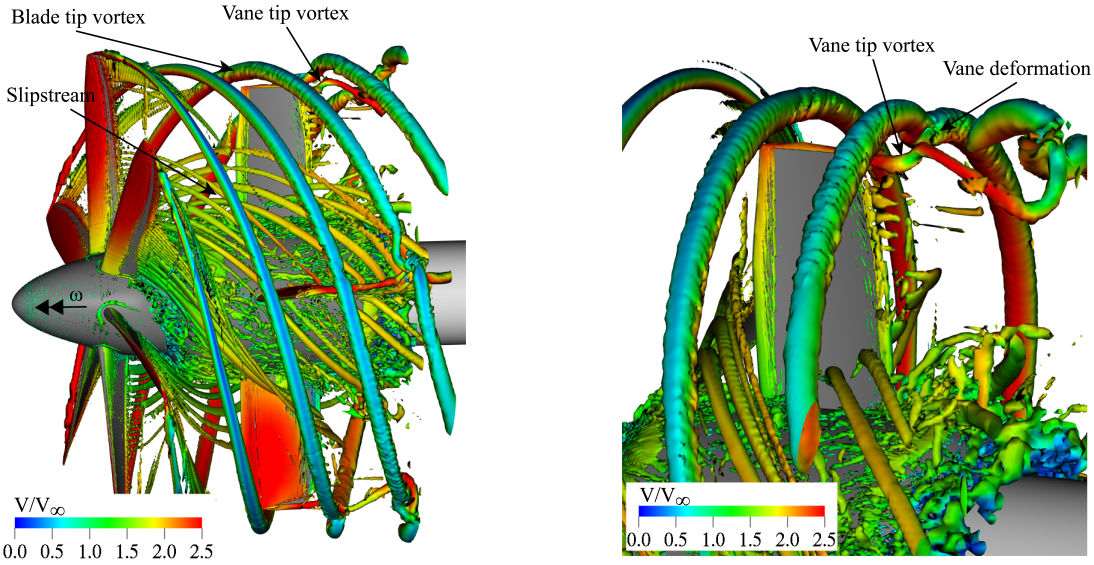

Fig. 22 Two views of the instantaneous flow field visualized through the λ_2 criterion for vortex visualization color contoured with the non-dimensional velocity magnitude.

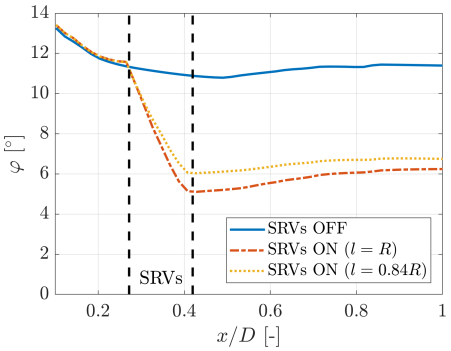

Fig. 23 Average swirl angle for the baseline and shorter vanes configurations along the axial direction.

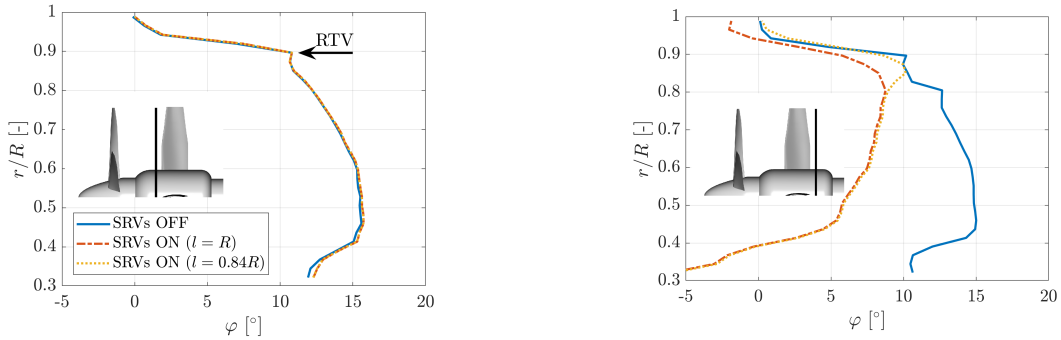

Fig. 24 Radial distribution of the time-averaged swirl angle ϕ in front (left) and behind (right) the SRV.

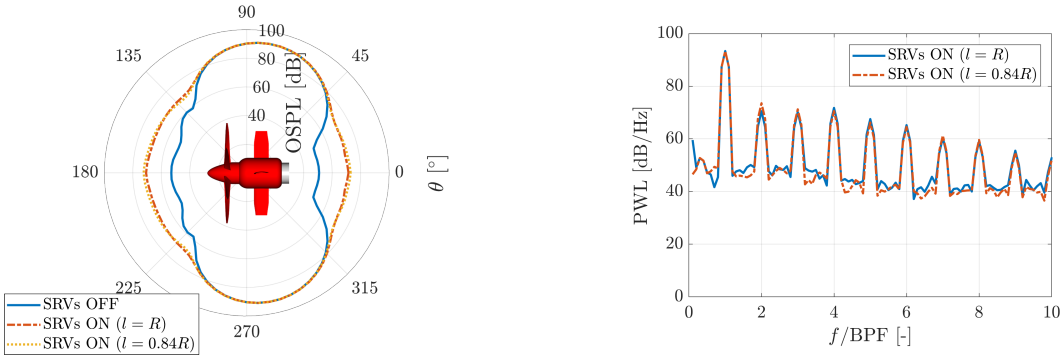

Fig. 25 (left) Directivity plot of the Overall Sound Pressure Level (OSPL) computed on a sphere of radius 20 R and centered at $x/D = 0.2$ integrated between 0.5 BPF and 10 BPF. (right) Sound Power Level (PWL) as a function of frequency non-dimensionalized with respect to the blade passing frequency (BPF).

investigate the effect on the acoustic, directivity plots of the OSPL and PWL versus the non-dimensional frequency are discussed (figure 25). The figures clearly show that shorter vanes do not have any effect on the acoustic field. Both the directivity plots of the OSPL and the PWL show overlapping curves. This confirms the previous observations that most of the noise is generated by the impingement of the slipstream at the leading edge and that the contribution of the impingement of the propeller tip vortex is negligible.

VI. Conclusions

A numerical investigation of a propulsion system constituted by a propeller with swirl recovery vanes is carried out using the lattice-Boltzmann method to investigate the relation between aerodynamics and acoustics. The baseline configuration is the same as the one of Li et al. [5], optimized for performance using a lifting line approach, for which reference computational and experimental data are available. Numerical results were validated against the available data to verify the accuracy of the computational methodology. A second swirl recovery vane geometry, obtained by shortening the vanes to avoid the impingement of the propeller tip vortices, is also investigated.

For the baseline configuration, the efficiency of the entire propulsive system increases by 2.4% with respect to the isolated propeller because of additional thrust generated by both the SRVs and the propeller. This is obtained by reducing the swirl angle in the near-field wake by 48%. Drawbacks of the installation of the SRVs is that the additional thrust shows large fluctuations caused by the impingement of the propeller wake on the SRVs. The impingement happens at a frequency equal to two times the BPF because the propeller tip vortex and the slipstream impinge in two different instants due to their different axial velocity.

It is found that most of the thrust is generated at the root of the SRVs, i.e. in the region interested by the impingement of the propeller slipstream, while the tip, i.e. the region subjected to the impingement of the tip vortex, contributes to only 1.9% of the SRVs thrust. The leading edge of the same region is the one that contributes the most to the far-field noise for which the dominant mechanisms is leading-edge impingement noise. The installation of SRVs causes noise

increase up to 20 dB only in the axial direction ($-30^\circ < \theta < 30^\circ$ and $120^\circ < \theta < 240^\circ$), because in the other directions propeller noise dominates. In the range of θ with noise increase, noise spectra of SPL present tonal peaks at frequencies harmonics of the second BPF caused by destructive interference between acoustic waves. For other θ angles, spectra show tonal peaks at frequencies harmonics of the first BPF . However, noise increase due to the swirl recovery vanes is negligible with respect to the overall isolated propeller noise that is 23 dB higher.

Shortening the vane length, to avoid the impingement of the tip vortex, causes a strong reduction of the thrust generated by the vane up to 13% with the baseline case, but no variation of the far-field noise. This suggests that the tip region of the vanes maintains the thrust distribution of the root part with very small noise penalty.

References

[1] Sinnige, T., Stokkermans, T., Ragni, D., Eitelberg, G., and Veldhuis, L., "Aerodynamic and Aeroacoustic Performance of a Propeller Propulsion System with Swirl-Recovery Vanes," *Journal of Propulsion and Power*, Vol. 34, No. 6, 2018, pp. 1376–1390. doi:10.2514/1.B36877, URL https://arc.aiaa.org/doi/10.2514/1.B36877.

[2] Guynn, M., Berton, J., Haller, W., Hendricks, E., and Tong, M., "Performance and Environmental Assessment of an Advanced Aircraft with Open Rotor Propulsion," Tech. rep., 2012. URL http://www.sti.nasa.gov.

[3] Stürmer, A., Marquez Gutierrez, C., Roosenboom, E., Schröder, A., Geisler, R., Pallek, D., Agoc, J., and Neitzke, K.-P., "Experimental and Numerical Investigation of a Contra Rotating Open-Rotor Flowfield," *Journal of Aircraft*, Vol. 49, No. 6, 2012, pp. 1868–1877. doi:10.2514/1.C031698, URL http://arc.aiaa.org/doi/10.2514/1.C031698.

[4] Li, Q., Wang, Y., and Eitelberg, G., "An investigation of tip vortices unsteady interaction for Fokker 29 propeller with swirl recovery vane," *Chinese Journal of Aeronautics*, Vol. 29, No. 1, 2016, pp. 117–128. doi:10.1016/J.CJA.2015.12.004, URL https://www.sciencedirect.com/science/article/pii/S1000936115002332.

[5] Li, Q., Öztürk, K., Sinnige, T., Ragni, D., Eitelberg, G., Veldhuis, L., and Wang, Y., "Design and Experimental Validation of Swirl-Recovery Vanes for Propeller Propulsion Systems," *AIAA Journal*, Vol. 56, No. 12, 2018, pp. 4719–4729. doi:10.2514/1.J057113, URL https://arc.aiaa.org/doi/10.2514/1.J057113.

[6] Wang, Y., Li, Q., Eitelberg, G., Veldhuis, L., and Kotsonis, M., "Design and numerical investigation of swirl recovery vanes for the Fokker 29 propeller," *Chinese Journal of Aeronautics*, Vol. 27, No. 5, 2014, pp. 1128–1136. doi:10.1016/J.CJA.2014.03.009, URL https://www.sciencedirect.com/science/article/pii/S1000936114000417.

[7] Gazzinga, J., and Rose, G., "Wind tunnel performance results of swirl recovery vanes as tested with an advanced high speed propeller," *28th Joint Propulsion Conference and Exhibit*, American Institute of Aeronautics and Astronautics, Reston, Virigina, 1992. doi:10.2514/6.1992-3770, URL http://arc.aiaa.org/doi/10.2514/6.1992-3770.

[8] Thom, A., and Duraisamy, K., "Computational Investigation of Unsteadiness in Propeller Wake–Wing Interactions," *Journal*

of Aircraft, Vol. 50, No. 3, 2013, pp. 985–988. doi:10.2514/1.C031866, URL http://arc.aiaa.org/doi/10.2514/1.C031866.

[9] Johnston, R. T., and Sullivan, J. P., "Unsteady wing surface pressures in the wake of a propeller," *Journal of Aircraft*, Vol. 30, No. 5, 1992, pp. 644–651. doi:10.2514/3.46393, URL http://arc.aiaa.org/doi/abs/10.2514/3.46393.

[10] Sinnige, T., de Vries, R., Della Corte, B., Avallone, F., Ragni, D., Eitelberg, G., and Veldhuis, L., "Unsteady Pylon Loading Caused by Propeller-Slipstream Impingement for Tip-Mounted Propellers," *Journal of Aircraft*, 2018. doi:10.2514/1.C034696.

[11] Casalino, D., Avallone, F., Gonzalez-Martino, I., and Ragni, D., "Aeroacoustic study of a wavy stator leading edge in a realistic fan/OGV stage," *Journal of Sound and Vibration*, Vol. 442, 2019, pp. 138–154. doi:10.1016/J.JSV.2018.10.057, URL https://www.sciencedirect.com/science/article/pii/S0022460X18307375.

[12] Dittmar, J., and Hall, D., "The effect of swirl recovery vanes on the cruise noise of an advanced propeller," *13th Aeroacoustics Conference*, American Institute of Aeronautics and Astronautics, Reston, Virigina, 1990. doi:10.2514/6.1990-3932, URL http://arc.aiaa.org/doi/10.2514/6.1990-3932.

[13] Casalino, D., Hazir, A., and Mann, A., "Turbofan Broadband Noise Prediction Using the Lattice Boltzmann Method," *AIAA Journal*, 2017, pp. 1–20. doi:10.2514/1.J055674, URL https://arc.aiaa.org/doi/10.2514/1.J055674.

[14] Gonzalez-Martino, I., and Casalino, D., "Fan Tonal and Broadband Noise Simulations at Transonic Operating Conditions Using Lattice-Boltzmann Methods," *2018 AIAA/CEAS Aeroacoustics Conference*, American Institute of Aeronautics and Astronautics, Reston, Virginia, 2018. doi:10.2514/6.2018-3919, URL https://arc.aiaa.org/doi/10.2514/6.2018-3919.

[15] Avallone, F., Casalino, D., and Ragni, D., "Impingement of a propeller-slipstream on a leading edge with a flow-permeable insert: A computational aeroacoustic study," *International Journal of Aeroacoustics*, Vol. 17, No. 6-8, 2018, pp. 687–711. doi:10.1177/1475472X18788961, URL http://journals.sagepub.com/doi/10.1177/1475472X18788961.

[16] Nardari, C., Casalino, D., Polidoro, F., Coralic, V., Lew, P.-T., and Brodie, J., "Numerical and Experimental Investigation of Flow Confinement Effects on UAV Rotor Noise," *25th AIAA/CEAS Aeroacoustics Conference*, American Institute of Aeronautics and Astronautics, Reston, Virginia, 2019. doi:10.2514/6.2019-2497, URL https://arc.aiaa.org/doi/10.2514/6.2019-2497.

[17] Succi, S., *The lattice Boltzmann equation for fluid dynamics and beyond*, 1st ed., Clarendon Press, Oxford, 2001.

[18] Shan, X., Yuan, X.-F., and Chen, H., "Kinetic theory representation of hydrodynamics: a way beyond the Navier–Stokes equation," *Journal of Fluid Mechanics*, Vol. 550, 2006, pp. 413–441. doi:10.1017/S0022112005008153, URL http://www.journals.cambridge.org/abstract{_}S0022112005008153.

[19] Chen, S., and Doolen, G., "Lattice Boltzmann method for fluid flows," *Annual Review of Fluid Mechanics*, Vol. 30, No. 1, 1998, pp. 329–364. doi:10.1146/annurev.fluid.30.1.329, URL http://www.annualreviews.org/doi/10.1146/annurev.fluid.30.1.329.

[20] Chen, H., Chen, S., and Matthaeus, W., "Recovery of the Navier-Stokes equations using a lattice-gas Boltzmann method," *Physical Review A*, Vol. 45, No. 8, 1992, pp. R5339–R5342. doi:10.1103/PhysRevA.45.R5339, URL https://link.aps.org/doi/10.1103/PhysRevA.45.R5339.

[21] Chen, H., Zhang, R., and Gopalakrishnan, P., "Lattice Boltzmann Collision Operators Enforcing Isotropy and Galilean Invariance," , aug 2015. URL https://patents.google.com/patent/US20150356217A1/en.

[22] Yakhot, V., and Orszag, S., "Renormalization group analysis of turbulence. I. Basic theory," *Journal of Scientific Computing*, Vol. 1, No. 1, 1986, pp. 3–51. doi:10.1007/BF01061452, URL http://link.springer.com/10.1007/BF01061452.

[23] Teixeira, C., "Incorporating Turbulence Models into the Lattice-Boltzmann Method," *International Journal of Modern Physics C*, Vol. 09, No. 08, 1998, pp. 1159–1175. doi:10.1142/S0129183198001060, URL http://www.worldscientific.com/doi/abs/10.1142/S0129183198001060.

[24] Wilcox, D., *Turbulence modelling for CFD (Third Edition)*, DCW Industries, Incorporated, 2006.

[25] Launder, B., and Spalding, D., "The numerical computation of turbulent flows," *Computer Methods in Applied Mechanics and Engineering*, Vol. 3, No. 2, 1974, pp. 269–289. doi:10.1016/0045-7825(74)90029-2, URL http://www.sciencedirect.com/science/article/pii/0045782574900292.

[26] Ffwocs Williams, J., and Hawkings, D., "Sound Generation by Turbulence and Surfaces in Arbitrary Motion," *Philosophical Transactions of the Royal Society of London A: Mathematical, Physical and Engineering Sciences*, Vol. 264, No. 1151, 1969. doi:10.1098/rsta.1969.0031.

[27] Farassat, F., and Succi, G., "A review of propeller discrete frequency noise prediction technology with emphasis on two current methods for time domain calculations," *Journal of Sound and Vibration*, Vol. 71, No. 3, 1980, pp. 399–419. doi:10.1016/0022-460X(80)90422-8.

[28] Brès, G., Pérot, F., and Freed, D., "A Ffowcs Williams - Hawkings Solver for Lattice-Boltzmann Based Computational Aeroacoustics," *16th AIAA/CEAS Aeroacoustics Conference*, American Institute of Aeronautics and Astronautics, Stockholm, Sweden, 2010, pp. AIAA 2010–3711. doi:10.2514/6.2010-3711, URL http://arc.aiaa.org/doi/10.2514/6.2010-3711.

[29] Najafi-Yazdi, A., Bres, G., and Mongeau, L., "An acoustic analogy formulation for moving sources in uniformly moving media," *Proceedings of the Royal Society A: Mathematical, Physical and Engineering Sciences*, Vol. 467, No. 2125, 2010, pp. 144–165. doi:10.1098/rspa.2010.0172, URL http://rspa.royalsocietypublishing.org/cgi/doi/10.1098/rspa.2010.0172.

[30] Casalino, D., "An advanced time approach for acoustic analogy predictions," *Journal of Sound and Vibration*, Vol. 261, No. 4, 2003, pp. 583–612. doi:10.1016/S0022-460X(02)00986-0.

[31] Li, Q., Liu, X., Eitelberg, G., and Veldhuis, L., "Numerical Investigation of Swirl Recovery Design for Propeller Propulsion Systems," *2018 Applied Aerodynamics Conference*, American Institute of Aeronautics and Astronautics, Reston, Virginia, 2018. doi:10.2514/6.2018-3648, URL https://arc.aiaa.org/doi/10.2514/6.2018-3648.